STRUCTURAL BIOLOGY

Elucidating the active δ-opioid receptor crystal structure with peptide and small-molecule agonists

Tobias Claff[1,2]*, Jing Yu[1,3,4,5]*, Véronique Blais[6], Nilkanth Patel[7], Charlotte Martin[8], Lijie Wu[1], Gye Won Han[7], Brian J. Holleran[6], Olivier Van der Poorten[8], Kate L. White[7], Michael A. Hanson[9], Philippe Sarret[6], Louis Gendron[6], Vadim Cherezov[7], Vsevolod Katritch[7], Steven Ballet[8], Zhi-Jie Liu[1,3], Christa E. Müller[2†], Raymond C. Stevens[1,7†]

Selective activation of the δ-opioid receptor (DOP) has great potential for the treatment of chronic pain, benefitting from ancillary anxiolytic and antidepressant-like effects. Moreover, DOP agonists show reduced adverse effects as compared to μ-opioid receptor (MOP) agonists that are in the spotlight of the current "opioid crisis." Here, we report the first crystal structures of the DOP in an activated state, in complex with two relevant and structurally diverse agonists: the potent opioid agonist peptide KGCHM07 and the small-molecule agonist DPI-287 at 2.8 and 3.3 Å resolution, respectively. Our study identifies key determinants for agonist recognition, receptor activation, and DOP selectivity, revealing crucial differences between both agonist scaffolds. Our findings provide the first investigation into atomic-scale agonist binding at the DOP, supported by site-directed mutagenesis and pharmacological characterization. These structures will underpin the future structure-based development of DOP agonists for an improved pain treatment with fewer adverse effects.

INTRODUCTION

Global opioid use has reached record levels (*1*), and especially the United States has seen the recent acute opioid epidemic cause drug overdose to become the main cause of accidental deaths (*2*). As a consequence, the development of alternatives to classical opioid painkillers with lower risk of abuse and overdose has become one of the highest priorities in healthcare (*3*).

The opioid receptor family consists of three G protein–coupled receptor (GPCR) subtypes: the μ-, κ-, and δ-opioid receptors (MOP, KOP, and DOP, respectively) (*4*). Both the unrivaled analgesic potency and the well-known adverse effects (e.g., addiction, tolerance, and respiratory depression) of approved opioid drugs are primarily mediated by the MOP (*5*, *6*). However, the other opioid receptors have been extensively investigated as attractive targets for safer treatment of chronic pain (*7*), and the DOP, in particular, has shown additional anxiolytic and antidepressant-like effects (*8*, *9*). This beneficial psychopharmacological profile together with its milder adverse effects put selective DOP agonists at the forefront of the development of superior opioid analgesics.

In 1975, it was discovered that the enkephalin pentapeptides act as the opioid receptors' endogenous ligands (*10*). Subsequently, opioid receptor subtype-selective peptides as well as multifunctional peptides targeting both opioid and non-opioid receptors were prepared and optimized (*11*, *12*). Within a series of compounds designed as dual opioid/neurokinin 1 receptor ligands, the potent peptide agonist KGCHM07 [H-Dmt-D-Arg-Phe-Sar-*N*-Me-3′,5′-$(CF_3)_2$-Bn] was developed (Fig. 1) and showed high affinities to both DOP and MOP (*13*). As an alternative to peptide- and morphine-derived ligands, previously unknown small molecules with piperazine scaffold were discovered as selective DOP agonists by compound library screening (*14*). Further optimization yielded the promising agonist DPI-287 (Fig. 1) that displayed reduced risk of inducing convulsions (*9*), which is a common complication of DOP activation (*15*).

Here, we report two agonist-bound crystal structures of the thermostabilized DOP in an activated state, and in complex with the peptide KGCHM07 at 2.8 Å resolution and the small-molecule DPI-287 at 3.3 Å resolution. These structures provide the first atomic-level insights into DOP activation by two structurally diverse DOP agonists. While the DOP inactive state has been characterized by crystal structures with a small molecule (*16*) and a peptide antagonist (*17*) bound to the orthosteric site, agonist recognition by the DOP has remained elusive, and the structural basis of DOP agonist selectivity is not fully understood. Moreover, both small-molecule agonists that have been cocrystallized with the MOP and KOP are based on morphinan scaffolds (*18*, *19*), limiting our understanding of agonist binding pocket interactions with other small molecules, such as DPI-287. Furthermore, the pharmacological properties of the DOP fusion construct used for crystallization (Fig. 1 and Supplementary Text) were extensively characterized and compared to those of the wild-type (WT) DOP to evaluate potential effects of thermostabilizing mutations on binding and downstream signaling (table S1), which additionally provides the first detailed pharmacological characterization of DPI-287.

[1]iHuman Institute, ShanghaiTech University, Ren Building, 393 Middle Huaxia Rd, Pudong, Shanghai 201210, China. [2]PharmaCenter Bonn, University of Bonn, Pharmaceutical Chemistry I, An der Immenburg 4, D-53121 Bonn, Germany. [3]School of Life Science and Technology, ShanghaiTech University, Shanghai 201210, China. [4]CAS Center for Excellence in Molecular Cell Science, Shanghai Institute of Biochemistry and Cell Biology, Chinese Academy of Sciences, University of Chinese Academy of Sciences, Shanghai 200031, China. [5]University of the Chinese Academy of Sciences, Beijing 100049, China. [6]Department of Pharmacology-Physiology, Faculty of Medicine and Health Sciences, Institut de Pharmacologie de Sherbrooke, Centre de Recherche du CHUS, Université de Sherbrooke, 3001 12e Avenue Nord, Sherbrooke, Quebec J1H 5N4, Canada. [7]Departments of Biological Sciences and Chemistry, Bridge Institute, USC Michelson Center for Convergent Bioscience, University of Southern California, Los Angeles, CA 90089, USA. [8]Research Group of Organic Chemistry, Departments of Chemistry and Bioengineering Sciences, Vrije Universiteit Brussel, Pleinlaan 2, B-1050 Brussels, Belgium. [9]GPCR Consortium, San Marcos, CA 92078, USA.
*These authors contributed equally to this work.
†Corresponding author. Email: christa.mueller@uni-bonn.de (C.E.M.); stevens@shanghaitech.edu.cn (R.C.S.)

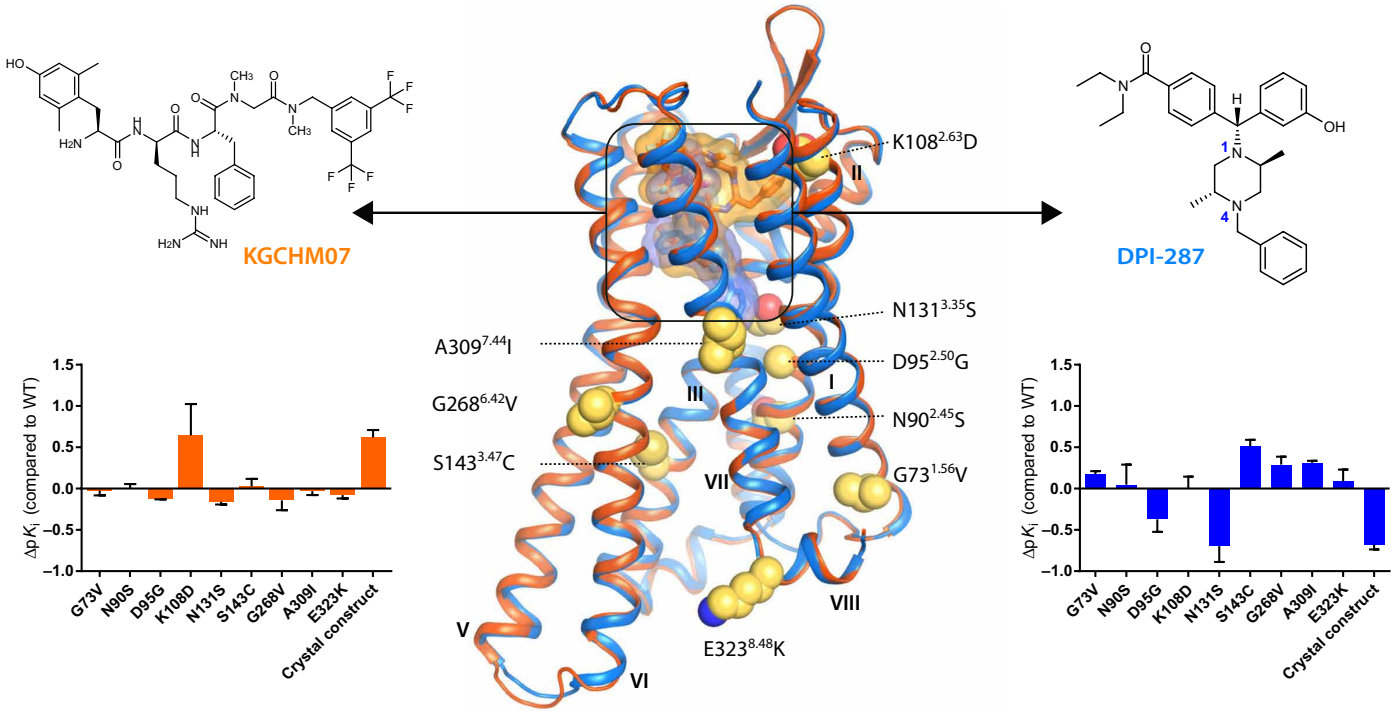

Fig. 1. Thermostabilized DOP construct without the N-terminal fusion protein, with both agonists KGCHM07 and DPI-287, used for crystallization, and effects of the crystal structure construct point mutations on the pK_i values of the agonists. The binding affinities (pK_i) of KGCHM07 (orange) and DPI-287 (blue) on membrane preparations of HEK cells expressing WT or mutant DOP constructs were determined by their ability to inhibit the binding of [^{125}I]-deltorphin I, used as a selective radioligand. Data were analyzed using a nonlinear fitting analysis, and the K_i values were calculated using GraphPad Prism 7.0. K_i values in the competition studies were determined from IC_{50} values using the Cheng-Prusoff equation and are represented as means ± SEM of three to six independent experiments, each performed in duplicate. Differences (delta) in pK_i values compared to WT are shown. The statistical significance was determined using a nonparametric one-way analysis of variance (ANOVA), showing that all pK_i differences of crystal construct mutants versus WT were statistically not significant ($P > 0.05$).

RESULTS

Activation-related changes in the DOP

Both agonist-bound structures are in an activated state. Unless otherwise indicated, we will use the higher-resolution BRIL-DOP-KGCHM07 structure for comparison with previously published inactive-state antagonist-bound DOP structures [Protein Data Bank (PDB) 4N6H and 4RWD] (*16*, *17*) and with active-state structures of the MOP (PDB 5C1M and 6DDF) (*18*, *20*) and KOP (PDB 6B73) (*19*). First, the agonist-bound DOP structures display large outward movements of the intracellular parts of helices V (4.5 Å) and VI (9.4 to 11.2 Å), and a 3.9 Å inward movement of helix VII (Fig. 2A), which is a common feature of the active conformational states of GPCRs (*21*). The shift of helix VII at the level of residue N314$^{7.49}$ [superscripts according to the Ballesteros and Weinstein numbering (*22*)] (Fig. 3A), which leads to a collapse of the allosteric sodium-binding pocket in active-state GPCR structures (*23*), is even more pronounced in the determined DOP structures as compared to the active MOP and KOP (Fig. 3B and fig. S1). However, this greater shift of N314$^{7.49}$ in the DOP might be affected by three mutations in the sodium-binding pocket (N90$^{2.45}$S, D95$^{2.50}$G, N131$^{3.35}$S) that were introduced during construct design. The activation-related outward movement of helix VI at the level of residue F270$^{6.44}$ is greater in the agonist-bound DOP than in the MOP and KOP. On the contrary, the very tips of helix VI (at position 6.28 as a reference) are more tilted by 4 to 6 Å in the active-state MOP and KOP (fig. S1), likely due to the bound G protein or nanobody, respectively, pushing helix VI tips further outward (*24*).

The rearrangements in the transmembrane helices are accompanied by several changes in the conserved microswitches that are typical for GPCR activation (*24*, *25*). Included are changes in the so-called P-I-F motif, where P225$^{5.50}$ moves inward by ~1.6 Å, forcing the I136$^{3.40}$ side chain to change its rotamer state and facilitating a major rotation of the bulky side chain of F270$^{6.44}$ (Fig. 2B) toward helix V by as much as ~3.5 Å at the Cγ atoms. For comparison, this movement is only ~2.6 Å in the active-state MOP and KOP structures. The P-I-F motif changes are coupled with rearrangements in the NP$^{7.50}$xxY motif, collapsing the sodium-binding pocket, with a ~3.5 Å inward shift of N314$^{7.49}$. Another residue of the sodium pocket and the NP$^{7.50}$xxY motif, Y318$^{7.53}$, switches its side-chain rotamer to a downward orientation, opening the intracellular entrance to the sodium pocket (Fig. 2C).

The overall conformation of the conserved DR$^{3.50}$Y motif remains largely unaltered between the active-like agonist-bound and the inactive-state DOP structures (Fig. 2C). Notably, the importance of the DRY motif in maintaining the inactive state in most GPCRs is attributable to a strong salt bridge between D$^{3.49}$ and R$^{3.50}$ residues. However, in all inactive-state structures of the DOP and other opioid receptors, this salt bridge is already disrupted, displaying distances of >3.5 Å. Moreover, the differences due to activation in the corresponding MOP and KOP structures manifest only in the side-chain reorientation of R$^{3.50}$ that directly interacts with the G protein (*20*) or nanobody (*18*, *19*), which are lacking in the DOP structures. To assess the activation state more rigorously, we evaluated the two

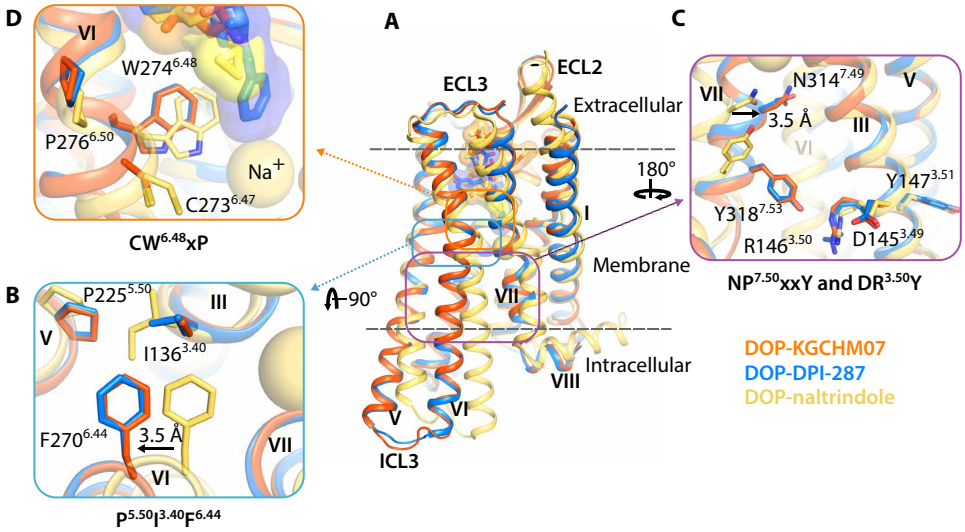

Fig. 2. Activation-related changes in the DOP. Comparison of conserved activation microswitches of the active-like DOP-KGCHM07 (orange) and DOP-DPI-287 (blue) structures with the inactive DOP-naltrindole structure (yellow, PDB 4N6H). Structural superposition of the (**A**) overall architecture, (**B**) PIF motif, (**C**) NPxxY and DRY motifs, and (**D**) CWxP motif.

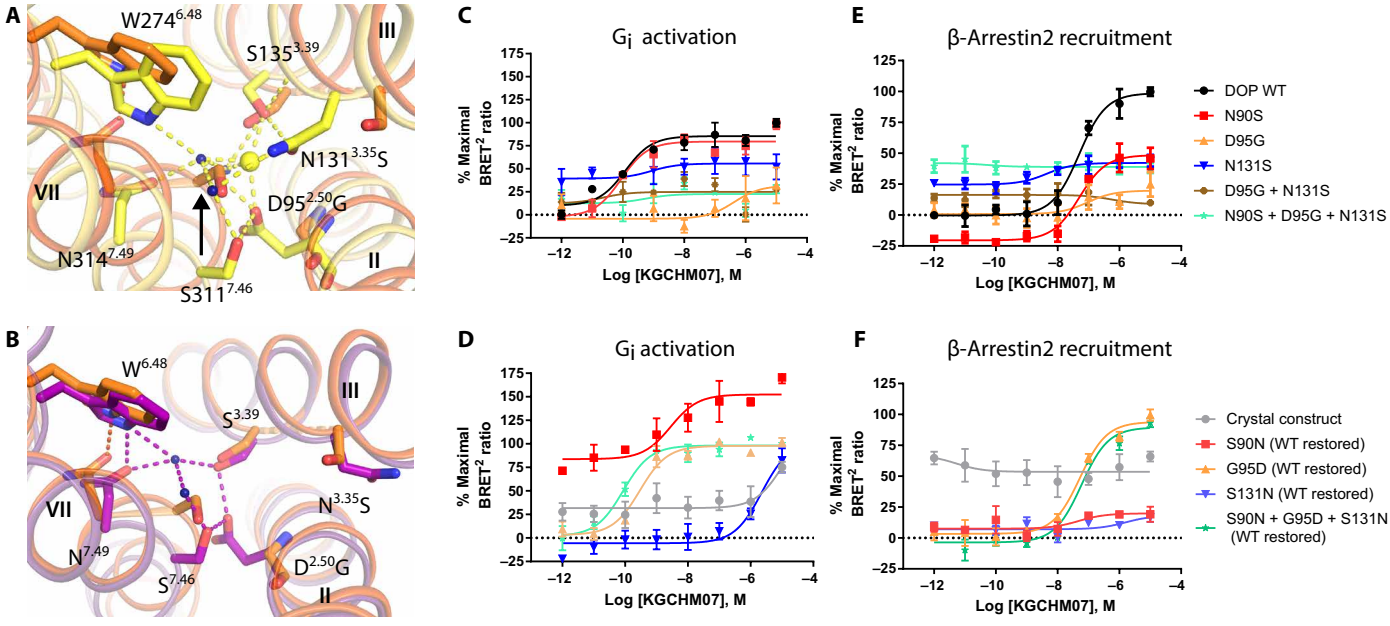

Fig. 3. Effects of sodium-binding mutations on receptor function. Comparison of the collapsed sodium-binding pocket in DOP-KGCHM07 (orange) with (**A**) inactive DOP (yellow, PDB 4N6H) and (**B**) active MOP (purple, PDB 5C1M) with perspective from the extracellular space. Water molecules are shown as blue spheres and the Na^+ ion as a yellow sphere. G_i-mediated cAMP signaling of (**C**) sodium-binding pocket mutants and (**D**) crystal structure construct mutants with sodium-binding pocket mutations restored to WT residues in response to different KGCHM07 concentrations (signals normalized to WT DOP). β-Arrestin2 recruitment of (**E**) sodium-binding pocket mutants and (**F**) crystal structure construct mutants with sodium-binding pocket mutations restored to WT residues in response to different KGCHM07 concentrations (signals normalized to the G95D mutant). Results are expressed as means ± SEM from $n = 4$ (EPAC) or $n = 3$ (β-arrestin2) independent experiments, each performed in triplicate.

new DOP structures along with previously solved opioid receptor structures for their activation-related conformations of microswitches using a GAUGE machine learning–based prediction tool (see Materials and Methods for details). All the microswitches in the new DOP structures, except the DRY motif, were predicted to be in the active-like or fully activated state (table S2).

Sodium pocket mutations allow receptor stabilization and control receptor function

The conserved site involved in binding of the negative allosteric modulator sodium in the DOP (*16*) was found to be collapsed in both agonist-bound DOP structures, similar to other class A GPCR structures determined in active or active-like states (Fig. 3, A and B)

(*18*, *23*). In our case, three mutations in the sodium pocket (N90$^{2.45}$S, D95$^{2.50}$G, N131$^{3.35}$S) apparently facilitated sodium expulsion and the collapse of the pocket, thereby stabilizing the receptor in an active-like state (Supplementary Text). A major decrease in thermostability was seen for agonist-bound DOP constructs lacking any of these mutations, which underlines their critical importance in thermostabilizing the agonist-bound DOP (fig. S2). However, the crystal construct retained high-affinity binding for KGCHM07 (K_i WT, 5.17 ± 1.57 nM; K_i crystal construct, 1.24 ± 0.23 nM), DPI-287 (K_i WT, 0.39 ± 0.12 nM; K_i crystal construct, 1.86 ± 0.23 nM), and [^{125}I]-deltorphin I (K_d WT, 1.11 nM; K_d crystal construct, 4.34 nM), indicating that the authenticity of the agonist-bound DOP binding pocket was not affected by the introduced point mutations (Fig. 1).

It is well established that mutations in the sodium-binding pocket can result in altered signaling properties (*16*), and our crystal structure construct lacked agonist-induced cyclic adenosine monophosphate (cAMP) response and β-arrestin2 recruitment (Fig. 3, C to F, and table S1). Our mutagenesis studies revealed that the DOP WT with the single point mutation D95$^{2.50}$G could be activated neither by KGCHM07 nor by DPI-287, while the agonist binding affinities were virtually unaltered (table S1). This is in contrast to a previously investigated D95$^{2.50}$A mutation that reduced the potency of the DPI-287–related agonist BW373U86 but maintained G protein signaling and β-arrestin recruitment (*16*). The G95$^{2.50}$D mutation in the crystal structure construct (reversing residue 2.50 back to WT) restored both cAMP and β-arrestin2 signaling fully (KGCHM07) or partially (DPI-287) (Fig. 3, C to F; fig. S3; and table S1).

Our mutagenesis experiments showed elevated basal responses in both cAMP and β-arrestin pathways for the single N131$^{3.35}$S and a triple DOP mutant (N90$^{2.45}$S, D95$^{2.50}$G, N131$^{3.35}$S), suggestive of a constitutively active receptor (Fig. 3, C to F, and fig. S3). In addition, when the signaling abilities of the crystal structure construct were evaluated, the baseline signal levels in both pathways were found to be higher than in the G95$^{2.50}$D mutant (used to normalize the crystal construct mutants) (Fig. 3, C to F, and fig. S3). To further assess the constitutive activity of the crystal structure construct, we performed a titration assay in which the amount of receptor construct DNA increased, while the levels of the biosensor (in this case $G_{\alpha i1}$-RLuc2 and $G_{\gamma 1}$-GFP10) remained constant (fig. S3). Increasing amounts of the crystal structure construct produced a decay of the signal, indicative of a ligand-independent dissociation of the G_i protein subunits induced by the receptor. A similar decay of the response signal was observed when the DOP WT construct was stimulated with DPI-287, further supporting that the crystal structure construct is constitutively activating the G_i protein signaling pathway.

A common denominator for opioid receptor activation

The new DOP structures provide atomic-level insights into the key components of molecular recognition for small-molecule and peptide agonists. Most of the opioid receptor ligands share a basic, protonated nitrogen atom forming a salt-bridge interaction to D128$^{3.32}$, which itself is connected to a polar network with potential involvement of Y308$^{7.43}$, T101$^{2.56}$, and Q105$^{2.60}$ linking helices II, III, and VII. In inactive-state DOP structures, this polar network can extend to Y109$^{2.64}$, involving water-mediated interactions. However, in activated structures, the Y109$^{2.64}$ side chain shows a large rotation toward helix I, uncoupling Y109$^{2.64}$ from the polar network, a mechanism that appears to be important for DOP activation. In the case of the DOP-DPI-287 complex, the distance for anchoring interactions between the protonated amine and D128$^{3.32}$ is ~3.0 Å. It is even greater (~3.5 Å) for the peptide KGCHM07, which shows multiple, direct, or potentially water-mediated interactions with D128$^{3.32}$ (Fig. 4, A and C). Another residue of the polar network, Y308$^{7.43}$, forms a direct hydrogen bond to the primary amine of the peptide KGCHM07, while Y308$^{7.43}$ does not interact directly with DPI-287's protonated amine (*N*4). In both structures, Y308$^{7.43}$ positioning is preserved by hydrogen bonds to D128$^{3.32}$, and in DPI-287 by additional π-π stacking interactions with the unsubstituted benzyl moiety (Fig. 4, B and C). At the same time, T101$^{2.56}$ helps in maintaining the polar network in the DOP-DPI-287 complex by forming hydrogen bonds with both Y308$^{7.43}$ and Q105$^{2.60}$, while the T101$^{2.56}$ side chain loses this interaction in the peptide-bound DOP-KGCHM07 complex, which uncouples it from the polar network (Fig. 4, A and C). D128$^{3.32}$ mutations to N or A virtually abolished KGCHM07 activity, while the potency of the small-molecule DPI-287 reduced 10-fold for D128$^{3.32}$N [half maximal effective concentration (EC_{50}), 0.060 nM versus 0.61 nM] and 30-fold for D128$^{3.32}$A (EC_{50}, 0.060 nM versus 1.39 nM) (Fig. 4D). Similarly, previous studies on opioid peptides reported that modifications of the N-terminal amine, including its acetylation or substitution by a methyl group, abolished agonistic activities while retaining low nanomolar affinity (*26*, *27*). However, we were unable to determine the affinity of KGCHM07 and DPI-287 for the D128$^{3.32}$ mutants, because no [^{125}I]-deltorphin I–specific binding could be observed (table S1).

The basic amines of KGCHM07 and DPI-287 are embedded deeper (1.9 and 1.4 Å, respectively) into the binding pocket when compared to the equivalent amines of the DOP antagonists DIPP-NH_2 (Fig. 4E) and naltrindole (Fig. 4F), resulting in the reorientation of the D128$^{3.32}$ side chain and the adjacent polar network. Furthermore, the MOP agonist BU72 (PDB 5C1M) shows the same 1.4 Å amine shift into the binding pocket when compared to a morphinan MOP antagonist (PDB 4DKL). Accordingly, the docking poses of 10 peptide and 7 small-molecule DOP agonists into our new active-like DOP structures (table S3) revealed that all respective amines were located deeper in the binding pocket when compared to DOP antagonists (Fig. 4, E and F, and fig. S4). Hydrophobic contacts with helix V or VII, or both, preclude antagonists such as DIPP-NH_2 and naltrindole to extend as deep into the DOP binding pocket as shown for DOP agonists (Fig. 4F and fig. S4). Therefore, we argue that the polar network around D$^{3.32}$ plays an essential role in agonist-induced activation at the DOP and propose that the positioning of the basic amine (as opposed to antagonists) deeper into the binding pocket is a hallmark of opioid agonist activity for ligands that contain a basic amine interacting with D$^{3.32}$.

Differences between peptide and small-molecule recognition by the DOP

Besides the abovementioned prevalent salt bridge formation, another important anchor of ligand interaction in opioid receptors is the phenol moiety that is conserved in many peptide and small-molecule ligands. Accordingly, the peptide agonist KGCHM07 contains the N-terminal tyrosine derivative 2,6-dimethyl-L-tyrosine (Dmt^1), which was shown to improve binding affinity and activity of peptidic ligands at opioid receptors (*28*). Its position is similar to the one observed for tyrosine in the active structure of MOP in complex with DAMGO [(D-Ala^2,*N*-Me-Phe^4, Gly-ol^5)-enkephalin] (*20*), but Dmt shows additional hydrophobic contacts in the DOP binding pocket. Three water molecules were found in the KGCHM07 binding

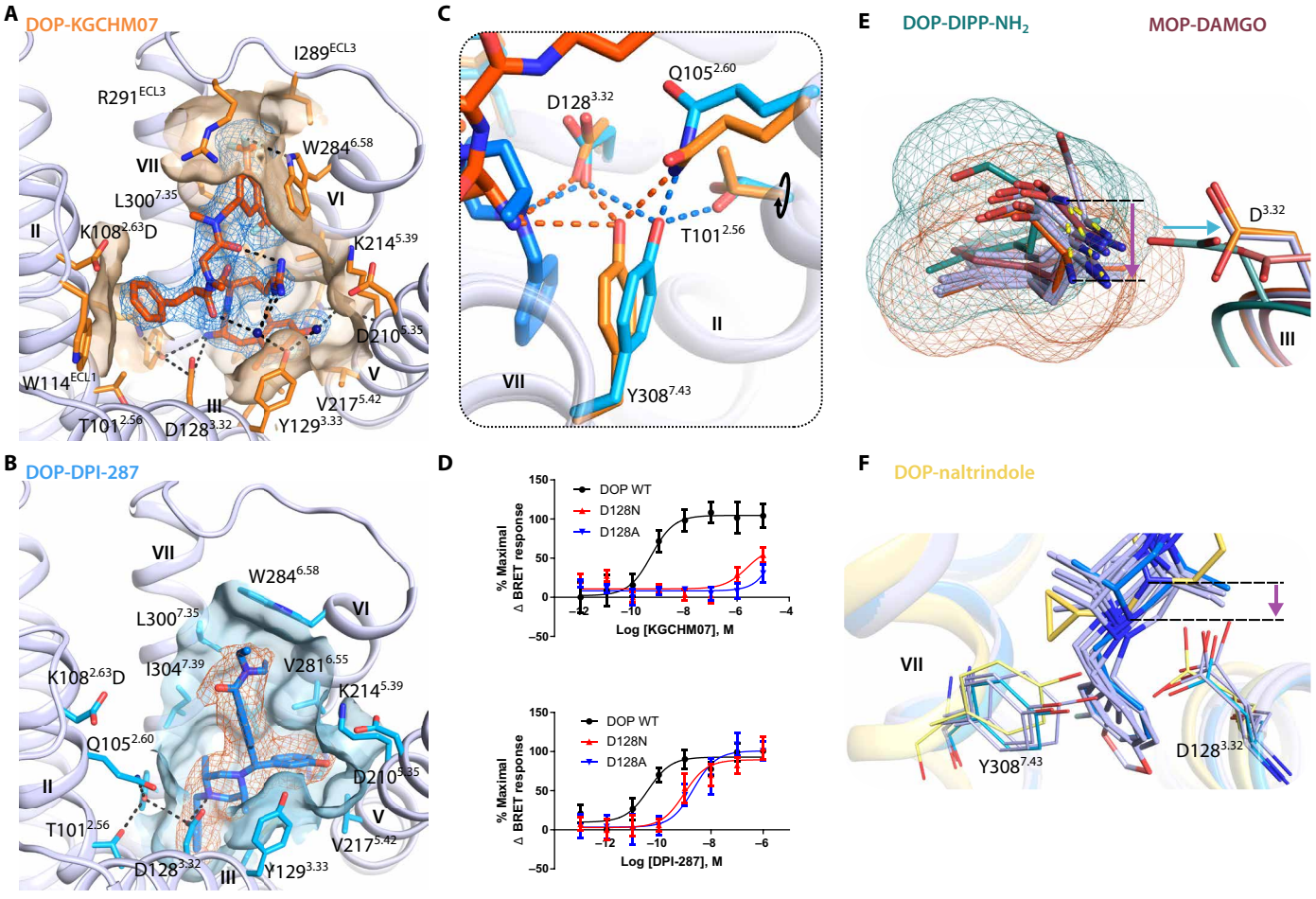

Fig. 4. Polar network around D128$^{3.32}$ and basic amine positioning as potential hallmark for opioid receptor activation. BRIL-DOP-KGCHM07, orange; BRIL-DOP-DPI-287, blue; naltrindole DOP antagonist structure (PDB 4N6H), yellow; DIPP-NH_2 DOP antagonist structure (PDB 4RWD), cyan; DAMGO MOP agonist structure (PDB 6DDF), red. (**A**) Overview of the KGCHM07 peptide binding pocket. The omit F_o-F_c electron density of KGCHM07 is shown in blue mesh (contoured at 3.0 σ). (**B**) Overview of the DPI-287 binding pocket. The omit F_o-F_c electron density of DPI-287 is shown in orange mesh (contoured at 3.0 σ). (**C**) Polar network anchoring the basic amine of DOP agonists. (**D**) G_i-mediated cAMP signaling of D128$^{3.32}$ mutants in response to different DOP agonist concentrations (upper panel, KGCHM07; lower panel, DPI-287). (**E**) Docking poses of DOP agonist peptides (gray) show that all primary amines embedded deeper into the binding pocket (yellow marks), when compared to antagonist DIPP-NH_2 (cyan) as indicated by the purple arrow. Similarly, the MOP-DAMGO complex (dark red) is displaced. The cyan arrow indicates related side movements of D$^{3.32}$. For clarity, only residue one (Phe^1 or Dmt^1) is depicted, and the surfaces of DOP agonist KGCHM07 and DOP antagonist DIPP-NH_2 are shown in orange and green mesh, respectively, to clarify its location in the binding pocket. (**F**) Docking poses of DOP small-molecule agonists (gray) show all substituted basic amines (*N*4) that penetrated deeper into the binding pocket, when compared to the antagonist naltrindole (yellow).

pocket, supported by weak electron densities (fig. S5). These are involved in connecting Dmt^1 to helices III, V, and VI via a polar interaction network with K214$^{5.39}$, H278$^{6.52}$, and Y129$^{3.33}$, which is also effectively connected to D-Arg^2 of KGCHM07 (Fig. 4A). Furthermore, our analysis suggests that the positively charged D-Arg^2 can form a water-mediated salt bridge interaction to D210$^{5.35}$ (fig. S5), supported by a 17-fold reduction in KGCHM07 binding to the D210$^{5.35}$N mutant. Moreover, [^{125}I]-deltorphin I, which was used as the radiotracer in these experiments, contains D-Ala^2 instead of D-Arg^2 and was not affected by D210$^{5.35}$ mutations (table S1). The lower resolution of the DPI-287 structure precluded robust identification of structural water molecules in this case. However, the energy-based prediction of water molecules suggested three tightly bound water molecules at residues H278$^{6.52}$ and Y129$^{3.33}$, linking DPI-287 to helices III, V, and VI as likewise observed in the KGCHM07-bound structure (fig. S5).

Our mutagenesis studies showed a binding decrease to the Y129$^{3.33}$F and Y129$^{3.33}$A mutants by ~7-fold and ~38-fold for KGCHM07 and by about 3-fold and about 5-fold for DPI-287, respectively (table S1). This finding confirms the involvement of Y129$^{3.33}$ in water-mediated polar networks in both structures. Similarly, the EC_{50} in a H278$^{6.52}$A mutant was reduced ~50-fold for KGCHM07 and ~10-fold for DPI-287. In addition, the backbone of K214$^{5.39}$ is also involved in this polar network, and a K214$^{5.39}$A mutant did not alter the potencies of KGCHM07 or DPI-287. However, single mutations of H278$^{6.52}$A and K214$^{5.39}$A abolished [^{125}I]-deltorphin I binding (table S1), indicating distinct binding pocket differences between the diverse agonists.

The Phe^3 side chain of KGCHM07 extends toward helices II and III and extracellular loop 1 (ECL1) and ECL2 and is positioned in a partially hydrophobic pocket formed by Q105$^{2.60}$, W114^{ECL1},

V124$^{3.28}$, L125$^{3.29}$, and C198^{ECL2} (Fig. 4A and fig. S4). In the designed DOP fusion protein, a K108$^{2.63}$D mutation was introduced (Supplementary Text) located at the extracellular entrance of the binding pocket. KGCHM07 binds to the K108$^{2.63}$D mutant with virtually unaltered affinity (table S1), and the docking of the KGCHM07 peptide into a DOP model with the K108$^{2.63}$ residue as in the WT receptor (table S3) suggests that KGCHM07 binds in the same pose as in the crystal structure. The flexible Sar^{4} residue of KGCHM07 adopts an energetically less favorable *cis*-amide bond to Phe^{3}, while all remaining amide bonds are found to be in the *trans*-conformation. This enables the C-terminal bistrifluoromethylated benzyl moiety to address the ECL3 region and extracellular ends of helices VI and VII. A large side-chain rotation of W284$^{6.58}$ by approximately 125°, compared to other DOP structures (Fig. 5, A and B, and fig. S4), opens a hydrophobic pocket consisting of I277$^{6.51}$, F280$^{6.54}$, V281$^{6.55}$, W284$^{6.58}$, I289^{ECL3}, R291^{ECL3}, and L300$^{7.35}$, harboring the benzyl moiety. This moiety is further stabilized by π-π stacking interactions and a hydrogen bond to W284$^{6.58}$ (Fig. 4A).

Structural basis for the selectivity of DOP agonists

The activated conformation of the DOP reveals contraction of the orthosteric binding pocket around the agonists. Helix VI moves into the agonist-binding pocket by 1.6 Å, while helix VII undergoes a 2.5 Å sideways movement (fig. S1). These helix movements close to the binding pocket result in conformational changes in the ECL3 region as compared to antagonist binding pockets. In the inactive state, R291^{ECL3} stabilizes the ECL3 region by forming hydrogen bonds with the carbonyl functions of V287$^{6.61}$ and W284$^{6.58}$ (Fig. 5A) (*16*). In the KGCHM07-bound structure, a large movement (10.0 Å based on the guanidine carbon) of R291^{ECL3} into the binding pocket can be observed, resulting in the disruption of this hydrogen bond network (Fig. 5B). The side chain of R291^{ECL3} is, therefore, more flexible in the agonist-bound DOP, and its electron densities only allowed us to model the full R291^{ECL3} residue in chain A of the BRIL-DOP-KGCHM07 structure, where it forms a lid over the hydrophobic pocket harboring KGCHM07's bistrifluoromethylated benzyl moiety. Although KGCHM07 is not DOP-selective because it also activates MOP (*13*), our BRIL-DOP-KGCHM07 structure reveals that R291^{ECL3} is accessible to the agonist binding pocket and is likely to play a role in the selectivity of DOP-binding peptides, as the MOP has a glutamic acid and the KOP has a histidine in the same position (Fig. 5D).

The small-molecule DPI-287 is ~10-fold selective for DOP over MOP (K_i DOP, 0.39 ± 0.12 nM; K_i MOP, 3.17 ± 0.27 nM). Our docking studies revealed that more selective analogs bind in the same binding pose as DPI-287, as described in the next section (Fig. 6), revealing that the *N*,*N*-diethylbenzamide moiety interacts with the nonconserved extracellular ends of helices VI and VII. The amide forms multiple hydrophobic contacts within a pocket consisting of V281$^{6.55}$, F280$^{6.54}$, W284$^{6.58}$, and L300$^{7.35}$ (Figs. 4B and 5C). Structural comparison with other opioid receptors reveals that the *N*,*N*-diethylbenzamide moiety of DPI-287 and analogs cannot occupy the same receptor space in the MOP and KOP as in the DOP due to steric interactions in positions 6.58 [charged in the case of MOP (K305) and KOP (E297)] and 7.35 (W320 in the MOP and Y312 in the KOP) (Fig. 5, C and D). Therefore, any larger substitution of L300$^{7.35}$ would prevent beneficial hydrophobic contacts due to steric clashes. On the other hand, replacing W284$^{6.58}$ with charged side chains would also make the subpocket less favorable for forming hydrophobic interactions.

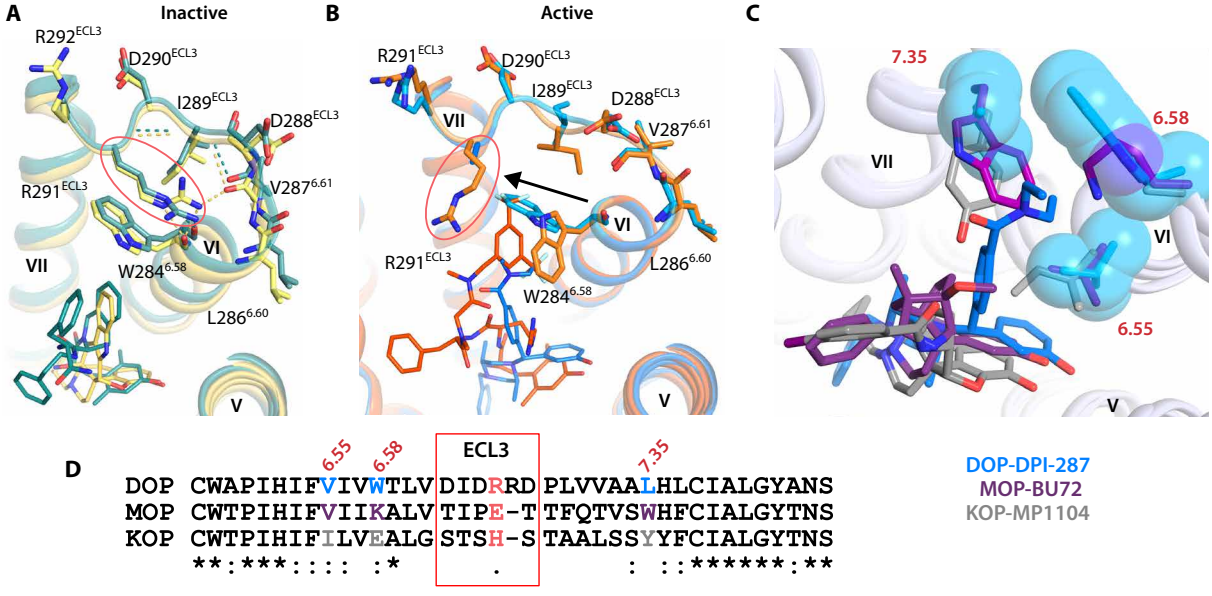

Fig. 5. Activation-related changes in the ECL3 region of the DOP and structural basis for DPI-287 selectivity. Comparison of ECL3 conformations between (**A**) inactive (naltrindole, yellow, PDB 4N6H and DIPP-NH_2, cyan, PDB 4RWD) and (**B**) active DOP binding pockets (DOP-KGCHM07, orange; DOP-DPI-287, blue). (**C**) Alignment of agonist-bound opioid receptor binding pockets. Pocket-forming residues are shown as sticks, with labels indicating Ballesteros-Weinstein nomenclature (*22*) and red numbers pointing to nonconserved residues. Note that the E$^{6.58}$ side chain of the KOP is not resolved in the KOP structure. (**D**) Opioid receptor sequence alignment of the nonconserved ECL3 (light red box) and the region close to the extracellular ends of helices VI and VII. The amino acids of MOP (E312) and KOP (H304) corresponding to DOP's R291 in the ECL3 region are highlighted in light red.

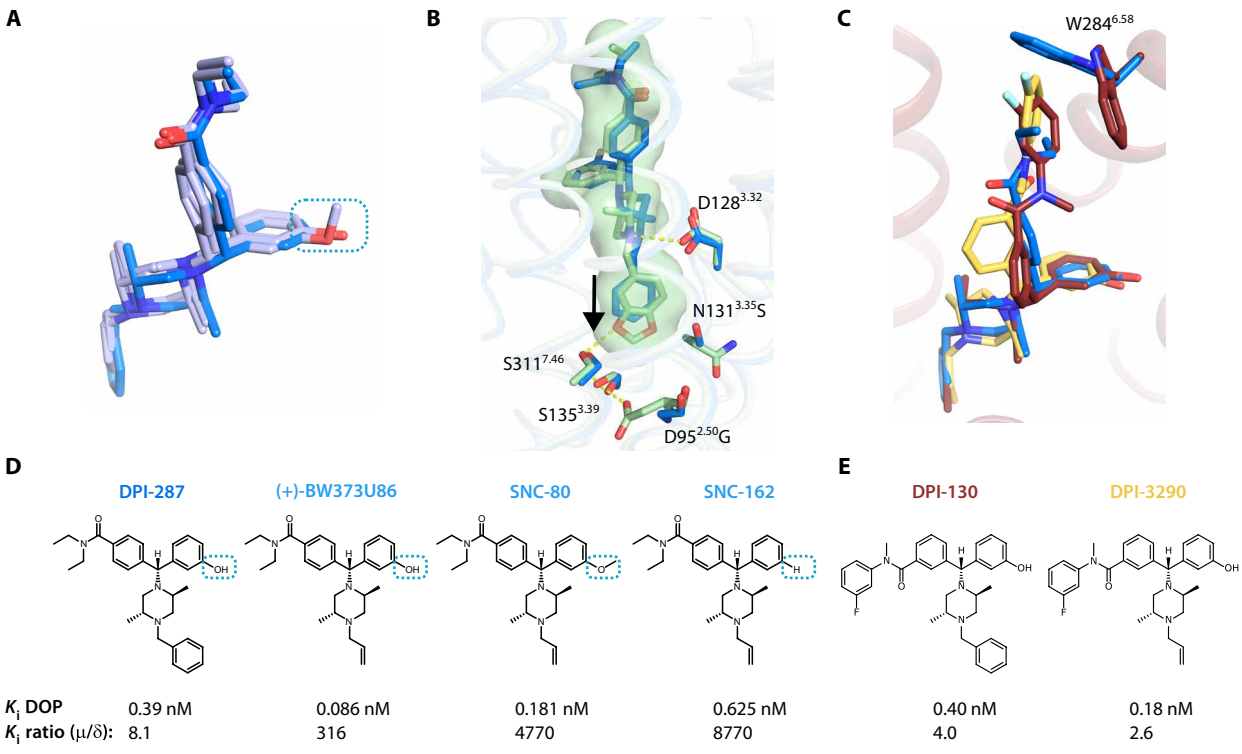

Fig. 6. Docking pose of DPI-287–related DOP agonists. (**A**) Alignment of the docking pose of the selected DPI-287 analogs BW373U86, SNC-80, and SNC-162 (all gray) with DPI-287 (blue). The blue box indicates the moiety with differences between these three docked analogs. (**B**) Docking pose of a DPI-287 analog with *N*-3,4-(methylenedioxy)benzyl substitution (green) and lacking the phenolic hydroxy function into a DOP model derived from the DOP-DPI-287 structure with G95$^{2.50}$D, S131$^{3.35}$N, and D108$^{2.63}$K reversed to WT, superimposed with DPI-287 (blue). The surface of the derivative is shown in green, and the black arrow indicates that the ligand is able to penetrate deeper into the entrance of the former sodium-binding pocket. (**C**) Superposition of the docking poses of DPI-130 (brown) and DPI-3290 (yellow) with DPI-287 suggests that the rotated W284$^{6.58}$ is essential for DOP binding. (**D**) Chemical structures and DOP binding properties (human opioid receptors) of (+)-BW373U86, SNC-80, and SNC-162 (*29*). (**E**) Chemical structures and binding properties (rat opioid receptors) of DPI-130 and DPI-3290 (*32*).

Structure-activity relationship of benzamide DOP agonists

The two new structures of DOP bound to a peptide and small-molecule agonist provide the structural basis for evaluating the key fingerprints that determine DOP selectivity. We performed molecular docking of several small-molecule analogs of DPI-287 at the DOP, MOP, and KOP (table S3). Docking of the selected DPI-287 analogs (+)-BW373U86, SNC-80, and SNC-162 (Fig. 6D) showed that these ligands assume the same orientation as that of DPI-287 with comparable docking scores at the DOP, whereas they exhibited much weaker docking scores at the MOP and KOP. Within this series of compounds, the phenolic hydroxy function of (+)-BW373U86 was either methylated (SNC-80) or removed (SNC-162), which interferes with their ability to form polar interactions. Previous work reported a reduced DOP affinity of these ligands by approximately twofold and approximately sevenfold, respectively, which is in agreement with the decrease of DPI-287 binding to mutants of Y129$^{3.33}$, one residue that interacts with the phenolic function of DPI-287 (table S1). Increased DOP selectivity was observed with phenolic moiety lacking (Fig. 6D) (*29*). However, the DOP docking poses of the respective benzyl moieties of SNC-80 and SNC-162 are overlapping with the phenol ring of DPI-287 in the new crystal structure (Fig. 6A), indicating that the water-mediated phenol interactions are not as important in the DOP as in the MOP.

(+)-BW373U86 differs from the cocrystallized DPI-287 only by its *N*4-allyl moiety but occupies the same position as DPI-287, while the allyl group overlaps with DPI-287's *N*4-benzyl moiety. In contrast, the bulkier *N*4-benzyl group of DPI-287 extends further into the entrance of the sodium-binding pocket. Conformational changes of W274$^{6.48}$ of the CW$^{6.48}$xP motif are essential for opening up the required space for the benzyl moiety (Fig. 2D). Moreover, it has been shown that substitution of the benzyl group with even larger residues like the *N*-3,4-(methylenedioxy)benzyl moiety (Fig. 6B) can be beneficial for DOP affinity (*30*). The docking pose of this analog reveals that it can penetrate further into the entrance of the sodium-binding pocket with only minor adjustment in the pocket-lining side chains, stabilized by a hydrogen bond to S311$^{7.46}$ (Fig. 6B). These findings indicate that the sodium-binding pocket can be targeted by ligand interactions in the DOP, as suggested for other GPCRs (*23*). However, the functional activity of ligands can be affected by further intrusion into the sodium pocket, as recently shown for the leukotriene B_4 receptor in complex with a bitopic ligand protruding deep into the sodium pocket. That ligand no longer activated the receptor but acted as an antagonist with inverse agonistic activity (*31*). The two *N*-(3-fluorophenyl)-*N*-methylbenzamide derivatives DPI-130 and DPI-3290 (*32*) differ from DPI-287 mostly in the bulkier benzamide moiety in the *meta*-position of the phenyl ring (Fig. 6E). Our docking studies show that the rotation of the W284$^{6.58}$ side chain, as observed in the DOP-KGCHM07 complex, can open up space for the 3-fluorophenyl moiety and stabilize it via π-π stacking interactions (Fig. 6C).

The piperazine ring of DPI-287 is represented in the energy-minimized chair conformation with axial methyl groups. Moreover, a conformational energy assessment predicted the axial methyl conformations as more favorable than the equatorial ones (−153.43 kJ/mol versus −109.81 kJ/mol). Methyl groups in the axial position are able to form hydrophobic contacts to Y129$^{3.33}$, M132$^{3.36}$, I304$^{7.39}$, and Y308$^{7.43}$, thereby perfectly occupying the additional binding pocket space. Furthermore, all docked analogs with the same *trans*-dimethyl substitutions showed axial methyl conformations (Figs. 4F and 6, A to C).

DISCUSSION

Here, two new active-like state DOP structures in complex with a peptide and a small-molecule agonist are presented at 2.8 and 3.3 Å resolution, respectively. We characterized both binding pockets and activation states by means of extensive pharmacological experiments and compared their binding poses to previously published opioid receptor structures. This approach allowed the determination of key factors for opioid receptor activation and DOP selectivity of *N*,*N*-diethylbenzamide derivatives, as well as crucial differences between peptide and small-molecule recognition.

Polar networks around the conserved D128$^{3.32}$ with rearrangements in the agonist-bound binding pocket are linked to DOP activation, which complements our understanding of opioid receptor activation. Similar interactions were observed in the active MOP (*18*) and KOP (*19*) structures. Furthermore, we observed that opioid agonists that contain a basic nitrogen interacting with D$^{3.32}$ extend deeper into the binding pocket as compared to structurally similar antagonists. Therefore, we suggest that the positioning of this basic nitrogen in the binding pocket and rearrangements in the polar network around D$^{3.32}$ are common denominators for opioid receptor activation by these ligands. This finding is in line with previous mutagenesis work (*33*). However, certain nonbasic ligands such as salvinorin A that are unable to form salt bridge interactions with D$^{3.32}$ are nonetheless able to activate opioid receptors (*34*), presumably by a unique activation mechanism involving hydrogen bonding to D$^{3.32}$ (*19*).

Moreover, we found substantial changes in the nonconserved ECL3 during activation, which makes R291^{ECL3} available for binding pocket interactions. The ECL3 region has been characterized as important for peptide agonist selectivity (*35*). The involvement of the nonconserved R291^{ECL3} seems reasonable and may represent a cationic counterpart for the carboxylate function of naturally occurring opioid peptides. This finding shows a possible interaction of R291^{ECL3} with the "address" moiety of endogenous peptides, based on the "message-address concept" proposed by Schwyzer in 1977 (*36*).

On the other hand, DOP-selective small molecules address the nonconserved extracellular ends of helices VI and VII with their *N*,*N*-diethylbenzamide moiety, providing a structural basis for DOP selectivity as this region is not similarly accessible in the MOP and KOP due to steric clashes. These findings are in agreement with previous data on DOP selectivity (*37*) and provide rational explanations that represent a substantial advance from our previous understanding. Moreover, the two new DOP structures have shed light on peptide recognition by the DOP. For instance, they revealed a large side-chain rotation of W284$^{6.58}$ in the peptide ligand binding pocket, allowing the peptide agonist KGCHM07 to access a larger subpocket with its C-terminal benzyl moiety. Our molecular docking studies show that the same pocket is probably also accessible for small molecules with bulkier amide substituents.

Together, our findings will be fundamental for DOP-centered, structure-based drug discovery programs in a time where opioid addiction–related deaths are markedly increasing, and safer opioid analgesics are urgently needed.

MATERIALS AND METHODS

Cloning, expression, and purification of the BRIL-DOP fusion protein

The construction of the DOP fusion protein gene was performed in a modified pFastBac1 vector as previously described (*16*). The amino acid residues 339 to 372 were truncated, and residues 1 to 40 were replaced with a thermostabilized apocytochrome b_{562}RIL from *Escherichia coli* (BRIL) containing the point mutations M7W, H102I, and R106L. A total of nine thermostabilizing point mutations were introduced into the DOP (G73$^{1.56}$V, N90$^{2.45}$S, D95$^{2.50}$G, K108$^{2.63}$D, N131$^{3.35}$S, S143$^{3.47}$C, G268$^{6.42}$V, A309$^{7.44}$I, and E323$^{8.48}$K). Eight of these mutations were transferred to the DOP from directed evolution experiments performed on the KOP (*38*). The engineered fusion protein was expressed in *Spodoptera frugiperda* (*Sf* 9) insect cells using the Bac-to-Bac Baculovirus Expression System (Invitrogen). Cells were infected at a density of 2 × 10^6 cells ml^{-1} and a multiplicity of infection of 5, and cell pellets were harvested 48 hours after infection for storage at −80°C. Insect cells were lysed by osmotic shock in hypotonic buffer supplemented with EDTA-free complete protease inhibitor cocktail tablets (Roche), and membrane pellets were washed repeatedly as previously described (*16*). Purified membranes were flash-frozen in liquid nitrogen and stored at −80°C after resuspension in a buffer containing 10 mM Hepes (pH 7.5), 10 mM $MgCl_2$, 20 mM KCl, and 30% (v/v) glycerol. Before solubilization, thawed membranes were incubated for 1 hour at 4°C in the presence of iodoacetamide (2 mg ml^{-1}) and either 25 μM DPI-287 (WuXi AppTec, Shanghai, China) or 100 μM KGCHM07 [synthesized as previously described (*13*)]. GPCRs were extracted from Sf9 membranes by solubilization over the course of 3 hours at 4°C in a final buffer composed of 55 mM Hepes (pH 7.5), 500 mM NaCl, 5 mM $MgCl_2$, 10 mM KCl, 15% (v/v) glycerol, 1.0% (w/v) *n*-dodecyl-β-D-maltopyranoside (DDM; Anatrace), 0.2% (w/v) cholesteryl hemisuccinate (CHS; Sigma), and either 12.5 μM DPI-287 or 50 μM KGCHM07. The supernatant was separated from insolubilized material by centrifugation at 60,000*g* for 30 min and incubated with 20 mM imidazole (pH 7.5) and 0.01 ml of TALON immobilized metal affinity chromatography resin beads (Clontech) per milliliter of supernatant overnight at 4°C. The resin was washed with 15 column volumes of wash buffer I [50 mM Hepes (pH 7.5), 600 mM NaCl, 0.1% (w/v) DDM, 0.02% (w/v) CHS, 10% (v/v) glycerol, 10 mM adenosine triphosphate (ATP), 10 mM $MgCl_2$, and either 25 μM DPI-287 or 50 μM KGCHM07] and 10 column volumes of wash buffer II [50 mM Hepes (pH 7.5), 600 mM NaCl, 0.02% (w/v) DDM, 0.004% (w/v) CHS, 10% (v/v) glycerol, 50 mM imidazole, and either 25 μM DPI-287 or 50 μM KGCHM07]. Last, the protein was eluted from the column with three column volumes of elution buffer [50 mM Hepes (pH 7.5), 600 mM NaCl, 0.01% (w/v) DDM, 0.002% (w/v) CHS, 10% (v/v) glycerol, 250 mM imidazole, and either 25 μM DPI-287 or 100 μM KGCHM07], and the protein was concentrated to 20 to 30 mg ml^{-1} using 100-kDa molecular weight cutoff centrifuge concentrators (Vivaspin, GE Healthcare). The resulting protein solution was directly used for crystallization trials, while monodispersity

and protein yield were determined by analytical size exclusion chromatography.

Crystallization

The purified and concentrated DOP construct bound to agonists was reconstituted into lipidic cubic phase by mixing the protein with a molten lipid mixture [10% (w/w) cholesterol and 90% (w/w) monoolein] in a 2:3 ratio using the two-syringe method (*39*). Crystallization trials were performed with an automatic crystallization robot (NT8, Formulatrix) by overlaying 50 nl of mesophase with 0.8 μl of precipitant solution on 96-well glass sandwich plates (NOVA catalog no. NOA90020, Hong Kong). The crystallization plates were stored at 20°C and imaged using an automatic crystal imager (RockImager 1000, Formulatrix). Crystals started to grow overnight and typically reached full size within 10 days of incubation. Diffraction quality crystals (length, 100 to 140 μm) of the BRIL-DOP-DPI-287 complexes were obtained in precipitant solutions composed of 32 to 35% (v/v) PEG-400 (polyethylene glycol, average molecular weight 400), 100 to 110 mM potassium citrate tribasic monohydrate ($C_6H_5K_3O_7{\cdot}H_2O$), and 100 mM MES (pH 6.0), whereas crystals (length, ~70 μm) of the BRIL-DOP-KGCHM07 complexes were obtained in precipitant solutions composed of 27 to 32% (v/v) PEG-400, 100 to 120 mM potassium citrate tribasic monohydrate ($C_6H_5K_3O_7{\cdot}H_2O$), and 100 mM MES (pH 6.0). Crystals were harvested using 50 to 100 μm of MicroMounts (MiTeGen) and flash-frozen in liquid nitrogen.

Data collection and structure determination

X-ray data collection was carried out at the SPring-8 beamline 41XU (Hyogo, Japan) using an x-ray minibeam (x-ray wavelength, 1.0000 Å) with a Pilatus 6M detector for the BRIL-DOP-KGCHM07 crystals (beam size, 11.0 × 9.0 μm^2), whereas an EIGER 16M detector was used for the BRIL-DOP-DPI-287 crystals (beam size, 10.0 × 9.0 μm^2). Automatic rastering and data collection were performed according to previously described strategies (0.1 s of exposure time and 0.1° rotation per frame with a total rotation of 5° to 10°) (*40*). For both the BRIL-DOP-DPI-287 and BRIL-DOP-KGCHM07 complexes, datasets from 23 crystals were integrated, scaled, and merged using XDS/XSCALE (*41*). An initial molecular replacement solution was obtained by PHASER (*42*) in the CCP4 suite, using the receptor portions of the DOP structure (PDB 4N6H), and BRIL from $A_{2A}AR$ (PDB 4EIY) as independent search models. The resulting BRIL-DOP model was refined by manually building in the excessive $2F_o$-F_c density and by repetitive cycling between COOT (*43*) and BUSTER (*44*) until convergence. Ten translation, liberation, and screw-rotation atomic displacement (TLS) groups were used throughout refinement. The elongated electron density tubes near the protein hydrophobic surface were modeled as oleic acids, with the exception of the few that were better fit with monooleins (OLC), the major lipid component used for crystallization. Regarding the BRIL-DOP-DPI-287 complex, 20 μM BMS986187 (Tocris Bioscience) was added as a positive allosteric modulator (PAM) to solve a potential allosteric pocket. However, no additional electron density for the copurified PAM BMS986187 could be observed in the BRIL-DOP-DPI-287 structure, while the overall structures from crystals that were generated with and without copurified PAM were highly similar with a root mean square deviation (RMSD) of 0.372 Å. An unidentified ~2 σ positive $2F_o$-F_c density between DPI-287 and helices II and III was observed in both structures solved from crystals with and without copurified PAM, which was a suspected artifact of crystal condition components. This observation remains unmodeled. The final DOP-DPI-287 complex structure contains DOP receptor residues 41 to 329 (chain A) and 43 to 333 (chain B) with two residues (−1 and 0, chain A) from expression tag, and BRIL residues 1 to 106 (chain A) and 3 to 100 (chain B). The refined DOP-KGCHM07 complex structure contains DOP receptor residues 41 to 329 (chain A) and 41 to 333 (chain B) with two residues (−1 and 0, chain A) from expression tag, and BRIL residues 1 to 106 (chain A) and 2 to 104 (chain B). The C-terminal tail of the B chain in both structures is involved in crystal packing with N-terminal residues of the A chain, which led to disrupted helices VII and VIII in the B chains. The data collection and refinement statistics are shown in table S4.

Molecular modeling of water molecules in the binding pocket

To further evaluate water-mediated interactions in the binding pocket of DOP-KGCHM07 and DOP-DPI-287 structures, we used the energy-based water prediction tool Sample Flood available in ICM-Pro version 3.8.7a (Molsoft) (*45*). Water predictions obtained from this procedure were further evaluated for stability in the given space by performing energy-based conformational minimization and sampling using water molecules and side chains of amino acid residues located within 4 Å of predicted water molecules for at least 100,000 Monte Carlo steps. Water molecules showing consistent conformations were further evaluated by comparison with electron density maps and considered further for docking and ligand interaction analysis.

Molecular docking

Selected opioid small-molecular ligands and peptide structures were obtained from the ChEMBL database (*46*). These ligands were further docked into the DOP-DPI-287 and DOP-KGCHM07 crystal structures using the docking platform available in ICM-Pro version 3.8.7a. The receptor structure complexes were preprocessed for docking to remove nonreceptor fusions. Water molecules inferred from water modeling using Sample Flood procedure implemented in ICM-Pro, and from the electron density data, were maintained in place while preparing receptor potential grid maps for docking. Ligand geometry was pre-optimized, and charge assignments were made using Merck Molecular Force Field (MMFF) (*47*). Conformational sampling and optimization in the docking process were performed using the biased probability Monte Carlo (BPMC) method with a sampling thoroughness of 50, beginning with a random seed conformation every time in at least three independent runs. The resulting docking poses were analyzed for their pose and interaction consistencies, and selected results were further analyzed. There were no distance restraints used to bias docking scores.

To revert the thermostabilizing mutations to WT residues in the docking models for a DPI-287 analog, the receptor coordinates from the DOP-DPI-287 complex structure were taken and the mutations around the ligand binding pocket $D95^{2.50}$, $N131^{3.35}$, and $K108^{2.63}$ were restored and the side chains were locally optimized using energy minimization–based refinement protocol in ICM-Pro. To account for the conformational changes, we further performed extensive energy minimization using BPMC protocol in ICM-Pro with at least 1,000,000 steps of conformational sampling and energy refinements. At the beginning of the refinement process, heavy atoms were restrained by soft harmonic tethers to the starting conformation to avoid large structural deviations, and then the tethers were gradually removed for the final refinement by reducing their weights. The refined structure had an RMSD value of 0.19 Å for all

C_α atoms compared to the DOP-DPI-287 complex and was further used for docking of a DPI-287 analog with *N*-3,4-(methylenedioxy) benzyl substitution using the abovementioned docking protocol.

Conformational state assessment with GAUGE

To assess the DOP structures in a rigorous and automated manner, we have developed a machine learning approach using class A GPCR structures available in the Protein Data Bank as a training set. Briefly, we selected a set of class A GPCR structures, in either fully active or inactive confirmations, and calculated distance-based descriptors for microswitches, including $P^{5.50}$-$I^{3.44}$-$F^{6.44}$, $D^{3.49}$-$R^{3.50}$-$Y^{3.51}$, and $N^{7.49}PxxY^{7.53}$ motifs and the conformations of the transmembrane helical domains near the intracellular region. Using this set of features and the annotated set of active and inactive structures as defined in the GPCRdb (*48*) as a training set, we applied a supervised machine learning approach to derive predictive models for each individual microswitch. We used support vector machines implemented in Python v.3.6 Scikit-learn library (*49*) for classification and regression to prepare models, to classify a given conformation as an active or inactive state, and to predict the extent of the activation by using regression models. For the assessment of DOP conformations, we used coordinates from the A chains of DOP-KGCHM07 and DOP-DPI-287. Nonreceptor fusions were removed, and the amino acid residues were mapped to their corresponding GPCRdb numbers (*50*). These structures were further used to calculate the set of corresponding descriptors as described above and used as an input for the prediction models to get the state assessment values (table S2). The method has the following advantages: (i) The scoring function in this tool includes conformational information from diverse class A GPCRs and is therefore less subjective than one representative structure. (ii) The regression models in this approach allow the evaluation of the extent of receptor activation on a scale from −1 (inactive) to 1 (active), derived from an analysis of known structures. (iii) By calculating individual scores at each major switch, one can detect special states that deviate from typical active or inactive states. For example, in the case of new active-state DOP structures, the GAUGE method detected that the DRY switch remains in the inactive state due to a lack of G protein or nanobody interactions with the receptor on the intracellular side.

Thermal shift assay

The protein thermostability of purified DOP constructs was assessed with a thermal shift assay using the thiol-specific fluorochrome *N*-[4-(7-diethylamino-4-methyl-3-coumarinyl)phenyl]maleimide (CPM). Stock solutions of CPM were prepared at 4 mg/ml in dimethyl sulfoxide and diluted 1:40 in buffer [25 mM Hepes (pH 7.5), 500 mM NaCl, 2% glycerol, 0.05% DDM, and 0.01% CHS] before usage. The reaction mixture was prepared in polymerase chain reaction (PCR) tubes of 0.2 ml capacity by mixing 1 μl of the diluted CPM stock solution with approximately 1 μg of purified protein in a total volume of 50 μl using the same buffer. Mixtures were incubated for 5 to 10 min, and protein thermostability was analyzed using a Rotor-Gene Q real-time PCR cycler (Qiagen) with an excitation wavelength of 365 ± 20 nm and a detection wavelength of 460 ± 20 nm (blue channel). The data of all samples were collected over a temperature range from 25° to 95°C with a temperature ramp of 1°C/min, and protein melting temperatures were determined using the Boltzmann sigmoidal fit (least squares) in GraphPad Prism 7.0 (GraphPad Software, San Diego, CA).

Radioligand binding assays

Binding assays were performed using membrane preparations from human embryonic kidney (HEK) 293 cells transiently transfected with 5 μg of DNA of the WT human DOP construct, or one of the various mutants of the full-length DOP or the BRIL-DOP crystal constructs. Cells (2.5×10^6) were transfected with X-tremeGENE HP (Sigma-Aldrich, Oakville, ON, Canada) in a 3:1 ratio using the manufacturer's protocol. Thirty-six hours after transfection, 58-cm^2 petri dishes were frozen at −80°C until use. On the day of the experiment, the cells were submitted to a heat shock by placing the petri dishes at 37°C for 60 s before returning them to ice. The cells were then harvested in 50 mM tris-HCl (pH 7.4) and centrifuged at 3200*g* for 15 min at 4°C. The protein concentration was determined with Bio-Rad DC Protein Assay reagents (Bio-Rad Laboratories, Mississauga, ON, Canada), and the pellet was further diluted in 50 mM tris-HCl (pH 7.4) buffer containing 0.1% bovine serum albumin (BSA) and distributed in 96-well plates. Saturation binding assays with 0.5 to 80 nM isotopically diluted [^{125}I]-deltorphin I were performed to determine the equilibrium dissociation constant (K_d) of each mutant for the radiotracer; 10 μM deltorphin I was used to define nonspecific binding. Determination of the affinity (K_i) of DPI-287 and KGCHM07 for DOP was achieved by competition binding assays with [^{125}I]-deltorphin I. The K_i values of the two compounds for DOP were determined using a membrane concentration of 20 to 40 μg of proteins per well and 1×10^5 counts per minute (cpm) of the radiolabeled ligand (specific activity, ~1700 Ci/mmol). Membranes and the radioligand were incubated for 60 min at room temperature with increasing concentrations of DPI-287 or KGCHM07 (0.1 pM to 10 μM). The reaction was then stopped by rapid vacuum filtration with ice-cold 50 mM tris-HCl (pH 7.4) on 96-well filter plates. Filters were then placed in 5-ml tubes, and the radioactivity was determined using the Wizard2 Automatic Gamma Counter (PerkinElmer, Woodbridge, ON, Canada). Data were analyzed using a nonlinear fitting analysis, and the K_i values were calculated using GraphPad Prism 7.0 (GraphPad Software, San Diego, CA). K_i values are expressed as means ± SEM from three to six independent experiments, each performed in duplicate. The affinity (K_i) of DPI-287 for MOP was achieved by competition binding assays with [^{125}I]DAMGO (specific activity, ~2200 Ci/mmol; K_d = 2 nM) and HEK cells expressing the human Flag-MOP (obtained from M. von Zastrow, University of California, San Francisco, CA). The K_i values in the displacement studies were determined from the half maximal inhibitory concentration (IC_{50}) values using the Cheng-Prusoff equation.

RLuc2-GFP10 BRET2-based biosensor assays

HEK293 cells were maintained in Dulbecco's modified Eagle's medium supplemented with 10% fetal bovine serum, penicillin (100 IU/ml), and streptomycin (100 μg/ml) at 37°C in a humidified 5% CO_2 atmosphere. For RLuc2-EPAC-GFP10 transfection, 500 ng of indicated receptor and 100 ng of RLuc2-EPAC-GFP10 per microgram of total transfected DNA were prepared in 150 mM NaCl. For β-arrestin2-GFP/receptor-RLuc2 transfection, 50 ng of WT and mutant crystallization construct BRIL-DOP or full-length DOP with RLuc2 cloned in the C terminus and 950 ng of β-arrestin2-GFP10 per microgram of total transfected DNA were prepared in 150 mM NaCl. For $G_{\alpha i1}$ biosensor assays, the indicated increasing amount of either DOP WT or BRIL-DOP crystal construct, 40 ng of G_α subunit, 250 ng of $G_{\beta 1}$ subunit, and 250 ng of $G_{\gamma 1}$ subunit per microgram of total transfected DNA were prepared in 150 mM NaCl.

Salmon sperm DNA was used to bring total transfected DNA to 1 μg, and each mixture was incubated for 20 min with 3 μg of polyethylenimine (Polysciences, Warrington, PA) per microgram of total transfected DNA before adding cells (350×10^3 cells/ml). Cells were plated at 35×10^3 cells per well in 96-well, flat-bottom, white opaque tissue culture plates. Forty-eight hours after seeding, cells were gently washed with stimulation buffer (10 mM Hepes, 1 mM $CaCl_2$, 0.5 mM $MgCl_2$, 4.2 mM KCl, 146 mM NaCl, and 5.5 mM glucose), and 80 μl of stimulation buffer was added to each well. Coelenterazine 400A (Gold Biotechnology Inc., St. Louis, MO) was added to a final concentration of 5 μM, 10 min before stimulation. For the EPAC (exchange protein directly activated by cAMP) assay, cells were stimulated with increasing concentrations of indicated ligand containing 3 μM forskolin (to increase cAMP) (Tocris Bioscience, Oakville, ON) for 10 min before signal acquisition. For β-arrestin2 assays, cells were stimulated with increasing concentrations of indicated ligand before signal acquisition. For $G_{\alpha i1}$ assays, cells were either unstimulated or stimulated with 100 nM DPI-287 for 5 min before signal acquisition. $BRET_2$ (bioluminescence resonance energy transfer 2) signals were measured using a TECAN M1000 fluorescence reader (TECAN, Grödig, Austria). RLuc2 and GFP10 emissions were collected in the 400- to 450-nm window (RLuc2) and 500- to 550-nm window (GFP10). The $BRET^2$ signal was calculated as the ratio of light emitted by the acceptor GFP10 over the light emitted by the donor RLuc2. For each assay, data were normalized as percentage of the maximal response for each ligand in the appropriate WT receptor background. All data were analyzed using the nonlinear curve fitting equations in GraphPad Prism 7.0 (GraphPad Software, San Diego, CA) to estimate the pEC_{50} values of the curves for the different pathways. Results are expressed as means ± SEM from $n = 4$ (EPAC) or $n = 3$ (β-arrestin2) independent experiments, each performed in triplicate.

Cell surface expression of the DOP

HEK293 cells (150×10^3) were transfected in suspension with 470 ng of DNA of the WT human DOP construct or one of the various mutants of the full-length DOP or the BRIL-DOP crystal constructs using X-tremeGENE HP 4:1 ratio in 24-well plates precoated with poly-L-lysine. Forty-eight hours after transfection, cells were fixed using a 3.7% formaldehyde/tris-buffered saline (TBS) solution. After 30 min of blocking with 1% BSA/TBS, the cells were incubated for 1 hour with a polyclonal anti-flag antibody (1:1000; Invitrogen, catalog no. 710662) followed by 1-hour incubation with anti-rabbit alkaline phosphatase (1:10,000; Sigma-Aldrich, catalog no. A3687). The level of expression of membrane DOP was detected using alkaline phosphatase substrate (Sigma-Aldrich, catalog no. S0942) in a solution containing 10% diethanolamine and 12.5 μM $MgCl_2$ (pH 9.8). The reaction was stopped by the addition of 0.4 M NaOH before reading absorbance at 405 nm using a TECAN M1000 multimode reader. Results are expressed as means ± SD from $n = 2$ independent experiments, each performed in triplicate.

SUPPLEMENTARY MATERIALS

Supplementary material for this article is available at http://advances.sciencemag.org/cgi/content/full/5/11/eaax9115/DC1

Supplementary Text

Fig. S1. Overall conformational changes of BRIL-DOP-KGCHM07 and BRIL-DOP-DPI-287 compared to other opioid receptor structures.

Fig. S2. The importance of sodium-binding pocket mutations and DOP agonists for protein thermostability.

Fig. S3. Effects of sodium-binding pocket mutations on DOP activation by DOP agonist DPI-287 and enhanced constitutive activity.

Fig. S4. Differences between ligand recognition with different scaffolds by the DOP.

Fig. S5. Water-mediated interactions during DOP activation.

Fig. S6. The crystal lattice of the active-like BRIL-DOP structures is arranged in antiparallel dimers.

Table S1. Pharmacological assessment of crystal structure construct mutants in WT (gray) or crystal structure construct background (blue) and ligand binding pocket mutants (green).

Table S2. Assessment of conformational states with the "GAUGE" tool for the DOP and other opioid receptor structures.

Table S3. Docking results for selected small-molecule and peptide DOP agonists.

Table S4. Data collection and refinement statistics.

View/request a protocol for this paper from *Bio-protocol*.

REFERENCES AND NOTES

1. S. Berterame, J. Erthal, J. Thomas, S. Fellner, B. Vosse, P. Clare, W. Hao, D. T. Johnson, A. Mohar, J. Pavadia, A. K. E. Samak, W. Sipp, V. Sumyai, S. Suryawati, J. Toufiq, R. Yans, R. P. Mattick, Use of and barriers to access to opioid analgesics: A worldwide, regional, and national study. *Lancet* **387**, 1644–1656 (2016).
2. D. H. Epstein, M. Heilig, Y. Shaham, Science-based actions can help address the opioid crisis. *Trends Pharmacol. Sci.* **39**, 911–916 (2018).
3. P.-Y. Law, P. H. Reggio, H. H. Loh, Opioid receptors: Toward separation of analgesic from undesirable effects. *Trends Biochem. Sci.* **38**, 275–282 (2013).
4. B. M. Cox, M. J. Christie, L. Devi, L. Toll, J. R. Traynor, Challenges for opioid receptor nomenclature: IUPHAR Review 9. *Br. J. Pharmacol.* **172**, 317–323 (2015).
5. R. J. Valentino, N. D. Volkow, Untangling the complexity of opioid receptor function. *Neuropsychopharmacology* **43**, 2514–2520 (2018).
6. H. W. Matthes, R. Maldonado, F. Simonin, O. Valverde, S. Slowe, I. Kitchen, K. Befort, A. Dierich, M. Le Meur, P. Dollé, E. Tzavara, J. Hanoune, B. P. Roques, B. L. Kieffer, Loss of morphine-induced analgesia, reward effect and withdrawal symptoms in mice lacking the μ-opioid-receptor gene. *Nature* **383**, 819–823 (1996).
7. L. Gendron, N. Mittal, H. Beaudry, W. Walwyn, Recent advances on the δ opioid receptor: From trafficking to function. *Br. J. Pharmacol.* **172**, 403–419 (2015).
8. L. Gendron, C. M. Cahill, M. von Zastrow, P. W. Schiller, G. Pineyro, Molecular pharmacology of δ-opioid receptors. *Pharmacol. Rev.* **68**, 631–700 (2016).
9. E. M. Jutkiewicz, The antidepressant-like effects of delta-opioid receptor agonists. *Mol. Interv.* **6**, 162–169 (2006).
10. J. Hughes, T. W. Smith, H. W. Kosterlitz, L. A. Fothergill, B. A. Morgan, H. R. Morris, Identification of two related pentapeptides from the brain with potent opiate agonist activity. *Nature* **258**, 577–580 (1975).
11. P. W. Schiller, Opioid peptide-derived analgesics. *AAPS J.* **7**, E560–E565 (2005).
12. J. V. Aldrich, J. P. McLaughlin, Opioid peptides: Potential for drug development. *Drug Discov. Today Technol.* **9**, e23–e31 (2012).
13. K. Guillemyn, P. Kleczkowska, A. Lesniak, J. Dyniewicz, O. Van der Poorten, I. Van den Eynde, A. Keresztes, E. Varga, J. Lai, F. Porreca, N. N. Chung, C. Lemieux, J. Mika, E. Rojewska, W. Makuch, J. Van Duppen, B. Przewlocka, J. Vanden Broeck, A. W. Lipkowski, P. W. Schiller, D. Tourwé, S. Ballet, Synthesis and biological evaluation of compact, conformationally constrained bifunctional opioid agonist–neurokinin-1 antagonist peptidomimetics. *Eur. J. Med. Chem.* **92**, 64–77 (2015).
14. K. J. Chang, G. C. Rigdon, J. L. Howard, R. W. McNutt, A novel, potent and selective nonpeptidic delta opioid receptor agonist BW373U86. *J. Pharmacol. Exp. Ther.* **267**, 852–857 (1993).
15. A. A. Pradhan, K. Befort, C. Nozaki, C. Gavériaux-Ruff, B. L. Kieffer, The delta opioid receptor: An evolving target for the treatment of brain disorders. *Trends Pharmacol. Sci.* **32**, 581–590 (2011).
16. G. Fenalti, P. M. Giguere, V. Katritch, X.-P. Huang, A. A. Thompson, V. Cherezov, B. L. Roth, R. C. Stevens, Molecular control of δ-opioid receptor signalling. *Nature* **506**, 191–196 (2014).
17. G. Fenalti, N. A. Zatsepin, C. Betti, P. Giguere, G. W. Han, A. Ishchenko, W. Liu, K. Guillemyn, H. Zhang, D. James, D. Wang, U. Weierstall, J. C. H. Spence, S. Boutet, M. Messerschmidt, G. J. Williams, C. Gati, O. M. Yefanov, T. A. White, D. Oberthuer, M. Metz, C. H. Yoon, A. Barty, H. N. Chapman, S. Basu, J. Coe, C. E. Conrad, R. Fromme, P. Fromme, D. Tourwé, P. W. Schiller, B. L. Roth, S. Ballet, V. Katritch, R. C. Stevens, V. Cherezov, Structural basis for bifunctional peptide recognition at human δ-opioid receptor. *Nat. Struct. Mol. Biol.* **22**, 265–268 (2015).
18. W. Huang, A. Manglik, A. J. Venkatakrishnan, T. Laeremans, E. N. Feinberg, A. L. Sanborn, H. E. Kato, K. E. Livingston, T. S. Thorsen, R. C. Kling, S. Granier, P. Gmeiner, S. M. Husbands, J. R. Traynor, W. I. Weis, J. Steyaert, R. O. Dror, B. K. Kobilka, Structural insights into μ-opioid receptor activation. *Nature* **524**, 315–321 (2015).

19. T. Che, S. Majumdar, S. A. Zaidi, P. Ondachi, J. D. McCorvy, S. Wang, P. D. Mosier, R. Uprety, E. Vardy, B. E. Krumm, G. W. Han, M.-Y. Lee, E. Pardon, J. Steyaert, X.-P. Huang, R. T. Strachan, A. R. Tribo, G. W. Pasternak, F. I. Carroll, R. C. Stevens, V. Cherezov, V. Katritch, D. Wacker, B. L. Roth, Structure of the nanobody-stabilized active state of the kappa opioid receptor. *Cell* **172**, 55–67.e15 (2018).
20. A. Koehl, H. Hu, S. Maeda, Y. Zhang, Q. Qu, J. M. Paggi, N. R. Latorraca, D. Hilger, R. Dawson, H. Matile, G. F. X. Schertler, S. Granier, W. I. Weis, R. O. Dror, A. Manglik, G. Skiniotis, B. K. Kobilka, Structure of the μ-opioid receptor–G_i protein complex. *Nature* **558**, 547–552 (2018).
21. D. Zhang, Q. Zhao, B. Wu, Structural studies of G protein-coupled receptors. *Mol. Cells* **38**, 836–842 (2015).
22. J. A. Ballesteros, H. Weinstein, Integrated methods for the construction of three-dimensional models and computational probing of structure-function relations in G protein-coupled receptors. *Methods Neurosci.* **25**, 366–428 (1995).
23. V. Katritch, G. Fenalti, E. E. Abola, B. L. Roth, V. Cherezov, R. C. Stevens, Allosteric sodium in class A GPCR signaling. *Trends Biochem. Sci.* **39**, 233–244 (2014).
24. V. Katritch, V. Cherezov, R. C. Stevens, Structure-function of the G protein–coupled receptor superfamily. *Annu. Rev. Pharmacol. Toxicol.* **53**, 531–556 (2013).
25. A. J. Venkatakrishnan, X. Deupi, G. Lebon, C. G. Tate, G. F. Schertler, M. M. Babu, Molecular signatures of G-protein-coupled receptors. *Nature* **494**, 185–194 (2013).
26. A. Ghosh, J. Luo, C. Liu, G. Weltrowska, C. Lemieux, N. N. Chung, Y. Lu, P. W. Schiller, Novel opioid peptide derived antagonists containing (2S)-2-methyl-3-(2,6-dimethyl-4-carbamoylphenyl)propanoic acid (2S)-Mdcp. *J. Med. Chem.* **51**, 5866–5870 (2008).
27. P. W. Schiller, I. Berezowska, T. M.-D. Nguyen, R. Schmidt, C. Lemieux, N. N. Chung, M. L. Falcone-Hindley, W. Yao, J. Liu, S. Iwama, A. B. Smith, R. Hirschmann, Novel ligands lacking a positive charge for the δ- and μ-opioid receptors. *J. Med. Chem.* **43**, 551–559 (2000).
28. D. W. Hansen Jr., A. Stapelfeld, M. A. Savage, M. Reichman, D. L. Hammond, R. C. Haaseth, H. I. Mosberg, Systemic analgesic activity and delta-opioid. selectivity in 2,6-dimethyl-Tyr1,D-Pen2,D-Pen5enkephalin. *J. Med. Chem.* **35**, 684–687 (1992).
29. R. J. Knapp, G. Santoro, I. A. De Leon, K. B. Lee, S. A. Edsall, S. Waite, E. Malatynska, E. Varga, S. N. Calderon, K. C. Rice, R. B. Rothman, F. Porreca, W. R. Roeske, H. I. Yamamura, Structure-activity relationships for SNC80 and related compounds at cloned human delta and mu opioid receptors. *J. Pharmacol. Exp. Ther.* **277**, 1284–1291 (1996).
30. D. R. Barn, A. Bom, J. Cottney, W. L. Caulfield, J. R. Morphy, Synthesis of novel analogues of the delta opioid ligand SNC-80 using $AlCl_3$-promoted aminolysis. *Bioorganic Med. Chem. Lett.* **9**, 1329–1334 (1999).
31. T. Hori, T. Okuno, K. Hirata, K. Yamashita, Y. Kawano, M. Yamamoto, M. Hato, M. Nakamura, T. Shimizu, T. Yokomizo, M. Miyano, S. Yokoyama, Na+-mimicking ligands stabilize the inactive state of leukotriene B_4 receptor BLT1. *Nat. Chem. Biol.* **14**, 262–269 (2018).
32. S.-p. Yi, Q.-h. Kong, Y.-l. Li, C.-l. Pan, J. Yu, B.-q. Cui, Y.-f. Wang, G.-l. Wang, P.-l. Zhou, L.-l. Wang, Z.-h. Gong, R.-b. Su, Y.-h. Shen, G. Yu, K.-J. Chang, The opioid receptor triple agonist DPI-125 produces analgesia with less respiratory depression and reduced abuse liability. *Acta Pharmacol. Sin.* **38**, 977–989 (2017).
33. A. Cavalli, A.-M. Babey, H. H. Loh, Altered adenylyl cyclase responsiveness subsequent to point mutations of Asp 128 in the third transmembrane domain of the δ-opioid receptor. *Neuroscience* **93**, 1025–1031 (1999).
34. B. L. Roth, K. Baner, R. Westkaemper, D. Siebert, K. C. Rice, S. Steinberg, P. Ernsberger, R. B. Rothman, Salvinorin A: A potent naturally occurring nonnitrogenous kappa opioid selective agonist. *Proc. Natl. Acad. Sci. U.S.A.* **99**, 11934–11939 (2002).
35. F. Meng, Y. Ueda, M. T. Hoversten, R. C. Thompson, L. Taylor, S. J. Watson, H. Akil, Mapping the receptor domains critical for the binding selectivity of delta-opioid receptor ligands. *Eur. J. Pharmacol.* **311**, 285–292 (1996).
36. R. Schwyzer, ACTH: A short introductory review. *Ann. N. Y. Acad. Sci.* **297**, 3–26 (1977).
37. C. Marie-Pepin, S. Y. Yue, E. Roberts, C. Wahlestedt, P. Walker, Novel "restoration of function" mutagenesis strategy to identify amino acids of the δ-opioid receptor involved in ligand binding. *J. Biol. Chem.* **272**, 9260–9267 (1997).
38. M. Schütz, J. Schöppe, E. Sedlák, M. Hillenbrand, G. Nagy-Davidescu, J. Ehrenmann, C. Klenk, P. Egloff, L. Kummer, A. Plückthun, Directed evolution of G protein-coupled receptors in yeast for higher functional production in eukaryotic expression hosts. *Sci. Rep.* **6**, 21508 (2016).
39. M. Caffrey, V. Cherezov, Crystallizing membrane proteins using lipidic mesophases. *Nat. Protoc.* **4**, 706–731 (2009).
40. V. Cherezov, M. A. Hanson, M. T. Griffith, M. C. Hilgart, R. Sanishvili, V. Nagarajan, S. Stepanov, R. F. Fischetti, P. Kuhn, R. C. Stevens, Rastering strategy for screening and centring of microcrystal samples of human membrane proteins with a sub-10 microm size X-ray synchrotron beam. *J. R. Soc. Interface* **6 Suppl. 5**, S587–S597 (2009).
41. W. Kabsch, XDS. *Acta Crystallogr. D Biol. Crystallogr.* **66**, 125–132 (2010).
42. A. J. McCoy, R. W. Grosse-Kunstleve, P. D. Adams, M. D. Winn, L. C. Storoni, R. J. Read, Phaser crystallographic software. *J. Appl. Cryst.* **40**, 658–674 (2007).
43. P. Emsley, B. Lohkamp, W. G. Scott, K. Cowtan, Features and development of Coot. *Acta Crystallogr. D Biol. Crystallogr.* **66**, 486–501 (2010).
44. O. S. Smart, T. O. Womack, C. Flensburg, P. Keller, W. Paciorek, A. Sharff, C. Vonrhein, G. Bricogne, Exploiting structure similarity in refinement: Automated NCS and target-structure restraints in BUSTER. *Acta Crystallogr. D Biol. Crystallogr.* **68**, 368–380 (2012).
45. R. Abagyan, M. Totrov, D. Kuznetsov, ICM—A new method for protein modeling and design: Applications to docking and structure prediction from the distorted native conformation. *J. Comput. Chem.* **15**, 488–506 (1994).
46. A. P. Bento, A. Gaulton, A. Hersey, L. J. Bellis, J. Chambers, M. Davies, F. A. Krüger, Y. Light, L. Mak, S. McGlinchey, M. Nowotka, G. Papadatos, R. Santos, J. P. Overington, The ChEMBL bioactivity database: An update. *Nucleic Acids Res.* **42**, D1083–D1090 (2014).
47. T. A. Halgren, Merck molecular force field. I. Basis, form, scope, parameterization, and performance of MMFF94. *J. Comput. Chem.* **17**, 490–519 (1996).
48. G. Pándy-Szekeres, C. Munk, T. M. Tsonkov, S. Mordalski, K. Harpsøe, A. S. Hauser, A. J. Bojarski, D. E. Gloriam, GPCRdb in 2018: Adding GPCR structure models and ligands. *Nucleic Acids Res.* **46**, D440–D446 (2018).
49. F. Pedregosa, G. Varoquaux, A. Gramfort, V. Michel, B. Thirion, O. Grisel, M. Blondel, P. Prettenhofer, R. Weiss, V. Dubourg, J. Vanderplas, A. Passos, D. Cournapeau, M. Brucher, M. Perrot, É. Duchesnay, Scikit-learn: Machine learning in Phyton. *J. Mach. Learn. Res.* **12**, 2825–2830 (2011).
50. V. Isberg, C. de Graaf, A. Bortolato, V. Cherezov, V. Katritch, F. H. Marshall, S. Mordalski, J.-P. Pin, R. C. Stevens, G. Vriend, D. E. Gloriam, Generic GPCR residue numbers – aligning topology maps while minding the gaps. *Trends Pharmacol. Sci.* **36**, 22–31 (2015).

Acknowledgments: The diffraction data were collected at the BL41XU of SPring-8 (JASRI proposals 2017A2708, 2017B2707, 2018A2561, and 2018B2721). We thank T. Hua, Y. Peng, K. Hasegawa, H. Okumura, and H. Murakami for their help with data collection. We thank the Cloning, Cell Expression, Assay, and Protein Purification Core Facilities of the iHuman Institute for their support. R.C.S. acknowledges that the University of Southern California is his primary affiliation. **Funding:** We thank the Shanghai Municipal Government, ShanghaiTech University, and GPCR Consortium for financial support. C.M., O.V.d.P., and S.B. thank the Research Foundation Flanders (FWO Vlaanderen) and the Research Council of the Vrije Universiteit Brussel for financial support. This work was supported by NIH grants R33DA038858 (V.K.) and P01DA035764 (V.K., V.C., and R.C.S.), as well as the Canadian Institute of Health Research (CIHR) (grant numbers MOP-123399 and MOP-136871) awarded to L.G. L.G. is the recipient of a Senior Salary support from the Fonds de Recherche du Québec—Santé. Funding from Shanghai covered the expression, crystallization, data collection, structure solution, and structure analysis research. Funding from the U.S. NIH supported the construct design and structure refinement/analysis. **Author contributions:** T.C., J.Y., V.B., N.P., C.M., L.W., G.W.H., B.J.H., and O.V.d.P. performed the experiments and analyzed the data. K.L.W., M.A.H., P.S., L.G., V.C., V.K., S.B., Z.-J.L., C.E.M., and R.C.S contributed to the study design, planning of the experiments, and interpretation of the data. T.C., J.Y., V.B., N.P., L.G., V.K., S.B., C.E.M., and R.C.S. wrote the manuscript; all other authors contributed to writing and revising the manuscript. **Competing interests:** V.C. is an author and editor at *Science Advances*. M.A.H. and R.C.S. are founders of ShouTi Pharma, a company focused on structure-based drug design for GPCRs. The authors declare that they have no other conflicts of interest. **Data and materials availability:** All data needed to evaluate the conclusions in the paper are present in the paper and/or the Supplementary Materials. Coordinates and structure factors have been deposited in the Protein Data Bank (PDB) under accession codes 6PT2 (BRIL-DOP-KGCHM07) and 6PT3 (BRIL-DOP-DPI-287). Other data are available from the corresponding authors upon reasonable request. Requests for the biosensors (RLuc2-EPAC-GFP10; $G_{\alpha i1}$-RLuc2 and $G_{\gamma 1}$-GFP10) should be submitted to M. Bouvier (michel.bouvier@umontreal.ca).

Submitted 3 May 2019
Accepted 25 September 2019
Published 27 November 2019
10.1126/sciadv.aax9115

Citation: T. Claff, J. Yu, V. Blais, N. Patel, C. Martin, L. Wu, G. W. Han, B. J. Holleran, O. Van der Poorten, K. L. White, M. A. Hanson, P. Sarret, L. Gendron, V. Cherezov, V. Katritch, S. Ballet, Z.-J. Liu, C. E. Müller, R. C. Stevens, Elucidating the active δ-opioid receptor crystal structure with peptide and small-molecule agonists. *Sci. Adv.* **5**, eaax9115 (2019).

Science Advances

Elucidating the active δ-opioid receptor crystal structure with peptide and small-molecule agonists

Tobias Claff, Jing Yu, Véronique Blais, Nilkanth Patel, Charlotte Martin, Lijie Wu, Gye Won Han, Brian J. Holleran, Olivier Van der Poorten, Kate L. White, Michael A. Hanson, Philippe Sarret, Louis Gendron, Vadim Cherezov, Vsevolod Katritch, Steven Ballet, Zhi-Jie Liu, Christa E. Müller and Raymond C. Stevens

Sci Adv **5** (11), eaax9115.
DOI: 10.1126/sciadv.aax9115